

**RECENT APPLICATIONS OF GASEOUS DISCHARGES:
DUSTY PLASMAS AND UPWARD-DIRECTED LIGHTNING**

A. Chutjian

Jet Propulsion Laboratory and California Institute of Technology
Pasadena, CA 91109

Intriguing phenomena have been recently observed in gaseous discharges which involve dust particles, and discharges which are produced in the ionosphere involving formation of upward-directed lightning. These phenomena abound here on earth and in astronomical objects. Dusty plasmas are found in laboratory RF generators such as used for microelectronics manufacture; in our planetary system as the stuff of rings and comets; and in planetary nebulae as nucleation sites for simple and complex molecules. Lightning occurs within planetary atmospheres [1,2] as well as in the earth's atmosphere and ionosphere. Lightning-accompanied upward-directed ionospheric discharges - so called *elves*, *red sprites*, and *blue jets* - have recently been detected in the earth's atmosphere by shuttle, aircraft, and ground observatories.

While these environments are seemingly different, they display a commonality due to the plasma. Electron attachment and ionization play key roles, their rates determined by species cross sections and by the electron-energy distribution function (*eedf*) in the plasma [3]. Negative-ion formation and surface charging lead to the growth, trapping, and crystallization of dust. In a thunderstorm cloud, the charge separation leading to lightning, the lightning electromagnetic pulse (EMP) itself, and the quasi-static electric fields (QSE) also establish an *eedf*, depending upon the *E*-field distribution, atmospheric composition, and altitude. Boltzmann transport equations are required for describing the electron and ion behaviors in both phenomena.

I Dust in Plasma Environments

Dust is found in a broad range of environments which include

combustion chambers, plasma discharges, thrusters, ion engines, gas lasers, comets, planetary magnetospheres, planetary rings, and the interstellar medium. Trapped dust affects the operation of semiconductor and micromachined devices either by altering the purity of the final etched surface or deposited layer, or by introducing grit into the micromachined structure. Dust also provides an additional high-area surface for heterogeneous chemical synthesis. It serves as a third body for chemical-bond formation involving neutral and/or ionized reactants, and absorbs part of the energy of bond formation, with another part remaining as kinetic, rotational, vibrational or electronic excitation available to the product species.

Two specific environments will be discussed. Negative ions play a role in the operation of weakly-ionized plasmas on earth [4]. They also play a role in molecule formation in the interstellar medium (ISM), especially with H and H₂. The interactions can be complex, eventually leading to the formation of complex species such as polyaromatic hydrocarbons (PAHs) using the "star stuff" (streaming and ejected neutrals and ions) of stellar winds, quasars, and supernovae [5]. In both the home-based and astronomical dusty plasmas, grains will in general be negatively charged. This follows from the requirement that the net fluxes of electrons and ions to a grain surface be zero. Assuming small, spherical grains (of diameter D smaller than the Debye length λ) and the absence of secondary electrons, the condition is,

$$[1 - eV_g/kT_i] = (m_i/m_e)^{1/2} \exp(eV_g/kT_e) . \quad (1)$$

Here m_i , T_i and m_e , T_e are the ion and electron masses and temperatures, respectively, e is the magnitude of electron charge, and V_g is the grain potential. For a simple case of protons and for $T_i = T_e = T$, one has the result that $V_g = -2.51kT/e$. Physically, plasma electrons generally travel faster than ions, hence their flux is greater, and the grain has to charge to a negative potential in order to repel enough electrons to maintain equality

with the positive-ion flux. In the more general case where electrons can be released from the grain via photoionization, ion sputtering, or secondaries produced from energetic electron-impact, the grain may be either positively or negatively charged. The sign of charge can also depend on the *local* temperatures and fluxes in a spatially distributed plasma, so that one can have regimes of alternating charge with an associated dipole or higher multipole moment.

I.1 Dust in Plasma-Processing Discharges

Discharges in methane (CH_4), silane (SiH_4), and germane (GeH_4) are routinely used in plasma processing to deposit hydrogenated-amorphous-silicon-germanium films (a-SiGe:H) and amorphous hydrogenated carbon films (a-C:H). These films have wide application in the manufacture of low band-gap solar cells, linear image sensors, thin-film transistors for liquid crystal displays, and in other microelectronic circuit components. The plasmas are rich in positive and negative ions [6], clusters [7], radicals [8-11], and dust particles [12-14]. Use of threshold ionization mass spectrometry has given information on total surface recombination probabilities [15,16]. The identification of the radicals and their density has also been studied in absorption using a hollow-cathode lamp or Ar^+ laser (intracavity) [12,14], and in emission [12,15]. As examples, the absorptions $\bar{X}^1A_1 \rightarrow \bar{B}^1B_2$ in SiH_2 , and $3p^2^1D_2 \rightarrow 3p4s^1P_1^\circ$ in Si; and the emissions $A^2\Delta \rightarrow X^2\Pi$ in SiH [17], and $4p5s^1P_1^\circ \rightarrow 4p^2^1D_2$ in Ge have been used to monitor the spatial density profiles a plasma, and surface recombination. A radiofrequency (RF) plasma reactor, consisting of circular capacitive plates, is combined with one or two polarized lasers to measure the Rayleigh light scattering from the generated particles. Several experimental arrangements may be found in Figs. 1 of Refs. [12] and [14]. Details of production of Si particles with diameters in the range 10-100 nm are given in Ref. [18].

The physics and chemistry of the plasma is determined by a

range of phenomena which includes elastic and superelastic electron collisions, ionization, two- and three-body electron attachment, dissociative excitation and ionization, positive ion-molecule collisions, negative ion-molecule collisions, metastable-state collisions, electron and ion recombination, and ion-ion neutralization. Surfaces play a role through secondary electron emission, heterogeneous reactions, and generation of ground-state, vibrationally-excited H_2 through recombination [19, 20]. A detailed discussion of these phenomena, including cross sections, rate constants, transport data, and method of solution to Boltzmann's equation for the SiH_4-H_2 discharge may be found in Perrin et al. [21] and Leroy et al. [22].

The spatial and temporal growth of particles with diameters in the range 1-100 nm is an intriguing phenomenon. A number of recent studies have been carried out on SiH_4 and GeH_4 discharge plasmas. Given here are just a few representative results using laser light scattering methods, combined with analysis of the spatial and temporal evolution of the laser light-scattering (LLS) intensity [23]. Shown in Fig. 1 is one apparatus used to measure the LLS intensity and evolution. The reactor consists of two plates (100 mm dia) separated by 45 mm. The bottom plate is grounded, and the RF power (about 3-30 MHz and 0.05-1.0 W/cm² power density) is impressed on the top electrode. Pure SiH_4 gas [23], or mixtures of SiH_4 and GeH_4 in Ar [11] have been used as the source gas. The light source is an argon-ion laser which is sometimes expanded into a rectangular beam for increased scattering volume. Scattered radiation is detected perpendicular to the directed beam using a scanning monochromator tuned to the incident Ar-ion wavelength (488 nm) or to one of the characteristic emission lines in the atom or radical listed above.

The density gradient of particles within the reactor in direction x normal to the electrode planes is described by the diffusion equation,

$$\frac{\partial n_p}{\partial t} = D \frac{\partial^2 n_p}{\partial x^2}, \quad (2)$$

where D and n_p are the diffusion coefficient and density, respectively, of the scattering particle [23]. The particle diameter D (and hence its mass from the known species density) is given by,

$$D = \frac{3}{2N_g(n^{1/3}d_{Si}+d_g)^2} \left[\frac{kT_g(nm_{Si}+m_g)}{2\pi nm_{Si}m_g} \right]^{1/2}, \quad (3)$$

where k is the Boltzmann constant; N_g , T_g and m_g are the density, temperature, and mass of the support gas; d_{Si} and m_{Si} are the density and mass of the Si atoms, and n is the number of atoms per Si dust particle. The time evolution of the plasma decay after the RF is turned off is measured at various positions x in the reactor, from which the second derivative $\partial^2 n_p / \partial x^2$ in Eq. (2), hence D in Eq. (3) are evaluated. Representative examples of the spatial distribution of Ar and Ge emissions for a GeH_4 -Ar plasma are shown in Fig. 2. The time evolution of particle density and size can be seen in Fig. 3 of Ref. [12]. These measurements are typically made through polarized laser light scattering measurements [24]. Here, the intensities I_{\parallel} and I_{\perp} of laser polarized parallel and perpendicular to an observation plane are measured. Combining these measurements with the absolute total laser-light scattering intensity and Mie scattering theory (requiring particle size distribution and complex refractive index) one obtains particle size and particle density [25,26]. In another photoemission method, laser light is used to photodetach electrons in negatively-charged particles, and to photoionize neutral particles. The increase in electron density is related to the electron affinity and the ionization potential of the target, which in turn are related to target size [27,28]. Results have been presented in targets of 1-100 Si atoms [29].

Several common threads of behavior exist in the silane and germane plasma for the spatial and temporal properties of particle

growth. These can be summarized as follows:

- particles are trapped, nucleate and grow at the plasma sheath boundary near the powered electrode
- radicals and atoms (GeH_2 , Ge, SiH, etc.) also have maximum concentration at the boundary
- short-lived radicals having high reactivity and production rate are the principal contributors to the initial growth of particles
- the initial particles are negatively charged or neutral, and can be electrostatically suspended in the plasma.

I.2 Suspension, Alignment and Ordering

One of the more fascinating aspects of dusty plasmas is the phenomenon of electrostatic suspension, alignment and crystal ordering. The forces acting on a dust grain are the resultant of the neutral drag, ion drag, electrostatic, gravitational, pressure-gradient, thermophoretic, and Stokes forces [4,30]. If the negatively-charged species has a charge q , interparticle distance d , and temperature T_i , then the coupling constant, defined as the ratio of the Coulomb and thermal energies, can be expressed as [31-33],

$$\Gamma = \frac{q^2}{4\pi\epsilon_0 kT_i d} \quad (4)$$

If the ratio Γ is of the order unity, the plasma is said to be strongly coupled. It can then exhibit unusual phenomena such as the formation of liquid and solid structures [33]. If the ratio Γ exceeds about 172 [34] a Coulomb lattice can be formed. In general, ordered structures are favored under conditions of large particle capacitance or negative charge (strong Coulomb attraction), low gas temperature (little disruption by collisions), and low gas density (low positive-ion density hence little Debye screening). Examples of hexagonal, bcc and fcc crystal structures have been reported by Chu and Lin I [33]. Use was made of a 14 MHz

reactor (1 W) and 0.2 torr mixture of O_2 and SiH_4 . Results are presented in Fig 3. From microimages and Langmuir-probe measurements of T_e , T_i , and N_i the plasma corresponds to a coupling parameter $\Gamma \approx 200$, in the right regime ($\Gamma \geq 170$) for a Coulomb cloud to be formed. Increasing the RF power resulted in a melting of the structures due to the reduced Debye screening. Dust grains of TiO_2 have also been suspended (gravitational + electrostatic forces) in a higher power (30W) 13.56 MHz discharge [35]. Formation of dust grains of diameter $20 \mu m$ with intergrain spacing $d = 880 \mu m$ were observed. By measuring the response of the cloud motion to a modulated dc bias, the total charge on the particle was determined. To see this one uses the force balance on the suspended charges written as [35],

$$m\ddot{x} + m\beta\dot{x} = qE(x) - mg + F_{ext}(t), \quad (5)$$

where x is the position of the particle in the sheath above the powered electrode, β is the damping constant, q, m are particle charge and mass, respectively, $E(x)$ is the time-averaged electric field, g is the gravitational constant, and $F_{ext}(t)$ is the force arising from the modulated bias on the powered electrode. Using Poisson's equation for $E(x)$, and solving Eq. (5) one obtains for the time-averaged particle's position,

$$x = x_0 + AR(\omega)\sin(\omega t + \phi), \quad (6)$$

where x_0 is the equilibrium position of the particle, and the second term in Eq. (6) is the response of the oscillator's amplitude, frequency and phase to the external modulation of the sheath boundary. Results are shown in Fig. 4 for the total charge as obtained by observing the resonant frequency and the amplitude factor. Agreement between the two approaches is good, and leads to total charges of about $q = -2 \times 10^5 e$ on an $18 \mu m$ diameter TiO_2 particle.

Further results have recently been reported in which fine carbon particles couple to generate *bcc* and *fcc* three-dimensional crystals, close to one another in space, or temporally [36].

"Melting" was induced by raising the reactor pressure, hence increasing the Debye shielding. Using dielectric (glass) microspheres of 1-50 μm diameter, Snyder et al. [37] have observed strings of glass beads aligned along the electric field direction. The strings in the plasma can be set in motion, independently of one another. The bonding is very likely through an induced bead-to-bead dipole moment. The combined electrical, gravitational and ion drag forces keep the particles at rest, with the electric field inducing a dipole moment on the resident particle charge [38]. It would be of interest to repeat these measurement with metallic spheres to give a different type of charge polarization in the dielectric.

I.3 Dust in Astronomical Plasmas

Dust is present throughout the universe, in the interstellar medium, ejected material from novae and supernovae, protostellar and protoplanetary accretion disks, and in planetary magnetospheres where material ejected from a moon of Jupiter or Saturn (by ion or particle impact) can lead to the brilliant and complex ring structures [39-43]. Dust is also a prominent part of comets, and recent Rosat satellite results have shown that sub-micron grains emerging from the comet surface can scatter solar X-ray radiation [44]. A dramatic photo (Fig. 5) taken with the Wide-Field Planetary Camera on the Hubble Space Telescope, shows a "star nursery" consisting of a weak plasma and dust, in which particles coagulate through charging and gravitational attraction to form new stars and planets.

Several reviewers have discussed the fundamental role played by dust in the physical processes extant in planetary magnetospheres, leading to tori (at Jupiter and Saturn) and planetary rings (at Jupiter, Saturn, Uranus and Neptune) via sputtering of surfaces [45,46]; and in cometary regions via a combination of solar radiation pressure, plasma drag (inelastic ion-surface collisions) and electromagnetic forces [39,41]. Dust

plays yet another role in the ISM by providing a surface for hydrogen atom recombination to form H_2 and other more complex species [5,47-49].

The equations of motion of a dust grain in the ISM or (taken here) in a stellar region are described by the force equation [40]

$$m\ddot{x} = q(E + v \times B) + F_g + F_d - \frac{\pi D^2}{4} P_{rad}. \quad (7)$$

Here, x is the grain position ($v = \dot{x}$), F_g is the star-grain gravitational force and F_d the Coulomb drag force between the grain and the local velocity of the plasma strain. P_{rad} is the radiation pressure exerted on the grain (of diameter D) by the star, which depends on the star's luminosity, the star-grain distance, and the grain albedo. The magnitude of the forces will depend on the local environment; as well as the direction of plasma flow (for F_c) which (for a planet) can be corotating with the planet, or (for a comet) in the direction of the solar wind. As pointed out by Goertz [40] for small grains the ratio R of electromagnetic force to gravitational force is $R = 2.5 \times 10^{-5} \phi_s \ll 1$ (for a $1 \mu m$ radius grain orbiting Saturn at a distance of two planetary radii). Hence these particles are primarily gravitationally bound. The grains are subject to azimuthal and radial electromagnetic forces in the planetary magnetosphere. Effects of changing surface charge (due to changes in the ambient magnetospheric plasma density and T), as well as changing B and E will also affect the grain's trajectory. A detailed three-dimensional fields-and-trajectories solution (much as one carries out in the design of charged-particle optics, with space charge!) is needed for any detailed study of grain dispersion [42,50].

The rate of interstellar formation of H_2 could not be explained by gas-phase collisions of H atoms because of low collision frequency for three-body relaxation collisions. One was then led to consider the role of dust grains in ISM molecular synthesis,

including the synthesis of H_2 [51,52]. In the classical Langmuir-Hinshelwood model of recombination [53], the mechanism of recombination involves the following steps: (a) a physisorptive or chemisorptive accommodation, (b) migration of the adsorbed H-atoms to one another, (c) chemical reaction in which the bond energy is now available for grain heating, and vibration (v)-rotation (J)-translation excitation of the molecules, and (d) ejection of the molecule from the surface in one or more v,J states. Details of the recombination kinetics are given by Levinson *et al.* [54], with extensions to superthermal collisions of H and H^+ on grains.

Considerable work is ongoing on the study of H-atom recombination relevant to RF plasma discharges [15,16]. Use has been made of temperature-programmed desorption (TPD) [53] in conjunction with threshold ionization mass spectrometry, and the surfaces studied have been stainless steel, α -Si:H, and oxidized Si. A recent example of laboratory work with an ISM-relevant target (olivine) at ISM temperatures (5-18 K) is that using fast atomic beams of H and D atoms to study the surface recombination to give HD [5,47-49]. A schematic diagram of this apparatus is given in Fig. 6. Thermal-energy beams of H and D are generated in two separate beam line using separate radio-frequency (RF) dissociation sources. After supersonic expansion, collimation, and three stages of differential pumping the beams impinge on a surface at UHV. The D_2 isotope is chosen to obviate problems of H_2 outgassing even from ultrahigh vacuum (UHV) stainless-steel vessels. The HD and D_2 production is monitored with a pumped, rotatable quadrupole mass analyzer, as a function of various parameters such as surface temperature, beam intensity, and exposure time. Corrections are made for various backgrounds of HD and D_2 due to vacuum-wall recombination, ambient (unpumped) density, and undissociated H_2 and D_2 in the incident beams. An example of a TPD curve of HD from an olivine (a mixture of Fe_2SiO_4 and Mg_2SiO_4) surface is given in Fig. 7 [48]. At the lowest coverage, the desorption kinetics are second order; *i.e.*, the H and D adsorbed atoms migrate towards each other and react as the surface warms, then desorb.

Based on these results, a modified expression for the recombination rate of surface-adsorbed H atoms has been proposed [5,48]. The recombination rate R (cm^3/s) is

$$R_{H_2} = \frac{1}{2}(S_H n_H v_H A \tau_H)^2 n_g \bar{N}^{-1} \nu f(T, a, \delta E) \gamma', \quad (8)$$

where S_H is the sticking fraction of H-atoms on the grain surface, n_H and v_H are the density and velocity of the gas-phase H-atoms, A is the average cross-sectional area of the grain, τ_H is the residence time of the atoms on the grain, n_g is the density of grains, \bar{N} is the average number of sites between two adsorbed H atoms, and γ' is the probability of bonding upon encounter. The factor $\nu f(T, a, \delta E)$ is the hopping rate of adatoms resulting from surface thermal kinetic energy and barrier tunneling, with an associated total barrier height a and width δE . Difficulties arise in accounting for the observed steep temperature dependence of the recombination efficiency [48,49] with expressions such as Eq. (8): the diffusion of H and D at the lowest T 's is slow, recombination depends strongly on surface T in the range 6-15 K, and the recombination is thermally activated. The sharp experimental behavior calls for an additional temperature dependence in γ' , or a high adatom surface density such that random walk is restricted. Further clarification of the mechanisms (random walk, barrier heights) influencing the T -dependence is needed.

Much of the well-characterized experimental work has been relevant to the diffuse ISM where H atoms are cooler. In addition, investigation of sticking coefficients for *superthermal* H and D atoms (energy range 0.1 - 10 eV, say) recombining on olivine grains would shed light on dust effects in shock-heated parts of the ISM, or in the vicinity of supernova remnants or starburst galaxies where energetic atoms are produced via shock heating, and charge exchange of fast outward-streaming ions with the neutral ISM. At these energies fast atoms can penetrate the bulk of the grain [54], and a TPD analysis may show the effects of bulk diffusion to the surface, followed by recombination and evaporation.

II **Elves, Red Sprites, and Blue Jets**

There was a large anecdotal history of observers having seen above giant thunderstorms continuous darts of light, upward-rising flames, luminous trails, and discharges with shapes of inverted tree roots [55]. These phenomena have undoubtedly been present from time immemorial, but the rapid and transient nature of the discharges made their recording and quantification (hence credibility) near-impossible until this century. A number of recent ground and aircraft campaigns [55-57] have provided further details into the interesting effects, some of which were predicted earlier [58]. The emissions with their characteristic colors and spatial extent arise through vertically- and horizontally-directed electric fields from lightning-driven electromagnetic pulses (EMP) [59-66]. The optical emissions have been termed *elves*, *red sprites* and *blue jets*. The characteristic colors are due to a predominance of various emission band systems in N_2 and N_2^+ . These bands are excited by the moderate energy electron-energy distribution function (e EDF) generated in the lightning. This e EDF usually peaks at about 1-2 eV, yet contains a tail of sufficient energy to ionize N_2 (threshold at 15.58 eV).

A schematic diagram of the ionospheric emissions structures is given in Fig. 8 [63,66]. *Elves* are an extended airglow appearing between $h = 70$ and 90 km altitude with a horizontal extent of several hundred km. *Red sprites* range from $h = 55$ - 80 km, with a width of about 20 - 30 km. Slender tendrils extend downward from about 55 km. *Blue jets* are born from the thunderstorm anvil top at 15 - 18 km, and propagate up to about 40 km altitude. The lifetimes of the emitters are of the order 0.1 ms, 10 ms, and 300 ms, respectively [63]. In addition, discharges called *blue starters* have been reported [67]. These are distinguished from *blue jets* by their lower terminal altitude, about $h = 25$ km vs 40 km for jets. It has been suggested that *blue starters* may also be wannabe *blue jets* ("proto blue jets") in which the ambient electric field E or cloud charge Q is insufficient to sustain ionization breakdown up

to $h = 40$ km [67,68].

Three scenarios have been presented for the production of sprites [62,63,66,69]. In each case electric fields produce acceleration of electrons, and an eedf is established by electron-neutral atmosphere collisions. This eedf is then used to compute the excitation rates of the various atomic and molecular components of the gas. The scenarios are (a) appearance of a large QSE field above a thundercloud after a lightning discharge, and propagating upward into the ionosphere, (b) excitation of species by an additional upward-propagating EMP pulse accompanying a large lightning discharge, and (c) possible excitation by accelerated runaway electrons produced via incident cosmic-rays ionization of the atmosphere within a thunderstorm cloud with its strong electric fields [70,71]. This last mechanism of runaway air breakdown can also give rise to blue-jet excitation, and the γ -ray flashes which have been observed by the BATSE instrument on the Compton Gamma Ray Observatory [70].

The red color of sprites results from a predominance of the first positive (1P) emission system in N_2 , the $B^3\Pi_g(v') \rightarrow A^3\Sigma_u^+(v'')$. Blue elves are made up of the second positive (2P) system, $C^3\Pi_u(v') \rightarrow B^3\Pi_g(v'')$. Vibrational quenching of the B state (red) is efficient for altitudes below about 50 km, hence the blue color is dominant in jets. A summary of the more commonly observed emission systems and processes is given in Table 1.

In all the high-altitude phenomena the energy drivers are the electric fields associated with the cloud charge separation and the lightning. The transient electric and magnetic fields have three sources. There is the field due to the initial charge distribution in the cloud (no discharge yet); an EMP from the propagation of the time-varying return stroke(s); and the QSE arising from the redistribution of charge after the return strokes. The time scale of these changes is approximately seconds or longer for establishing the initial charge distribution, 10^{-4} sec for the EMP,

and 10^{-3} sec for the redistribution and the QSE.

The neutral atmosphere is affected via electron-neutral collisions in which electrons of a time-varying eedf excite the most-abundant species N_2 and O_2 . Excitations here include direct collisional (electron) excitation to the many electronic states of N_2 lying below about 13 eV above the ground state, ionization-excitation to states of N_2^+ between 16 and 19 eV, and direct vibrational excitation of N_2 $X(v'')$ followed by v-v transfer to CO_2 , to give rise to 4.26 μm infrared radiation [CO_2 (001) \rightarrow (000)] transition (Table 1). An alternate, or possibly parallel heating mechanism can be through generation of high-energy electrons in the runaway regime, followed by acceleration to MeV energies with further secondary-electron generation [71]. The effects of atmospheric transmission by O_2 , O_3 and H_2O , as well as effects of excited-state quenching, will determine the spectral characteristics of the sprites and jets [69].

A three-dimensional time-dependent model has been developed by Ma et al. [65] to solve for the electric field, charge density, and Maxwell current. The last quantity is influenced primarily by the spatially anisotropic (tensor) conductivity in the ionosphere. The Maxwell's equations for the transient fields into the ionosphere are reduced into two equations. One is the wave equation,

$$\frac{\nabla \rho}{\epsilon} - \nabla^2 E = -\mu \sigma \frac{\partial E}{\partial t} - \mu \epsilon \frac{\partial^2 E}{\partial t^2}. \quad (9)$$

where ρ is the charge density (C/m^3), the dielectric constant (F/m), σ the conductivity tensor (S/m), μ the permeability (H/m , where $B = \mu H$), and E the electric field (V/m). The continuity of electrical current may be derived from the Maxwell's equation for $\nabla \times H$, in the form

$$\frac{\sigma \rho}{\epsilon} + \nabla \sigma \cdot \mathbf{E} + \frac{\partial \rho}{\partial t} - \frac{\partial \rho_s}{\partial t} = 0, \quad (10)$$

where ρ_s is the source charge density distribution carried by the return stroke. Equations (a) and (b) show the strong dependence of \mathbf{E} on the details of the ionospheric conductivity profile. One example of the profile σ vs altitude, at three conditions of latitude and time, is given in Fig. 9.

This upward-directed electric field accelerates the ambient thermal-energy electrons, of mean energy $\epsilon = 3/2kT$, to a new eedf which depends upon the local \mathbf{E} -field and neutral density. The connection between the spatial \mathbf{E} -field and the eedf is made through solution of either the Boltzmann equation [72] or the derived Fokker-Planck equation [73]. In either case, a full range of electron-molecule (N_2 , O_2) excitation, ionization (both direct and dissociative), and attachment (for O_2) cross sections are needed for meaningful solutions. Electron-ion and electron atom (N , O) scattering is usually neglected due to the small product of electron and ion or atom densities. Following the treatment of Taranenko et al. [74,75] (see also the analysis of Ref. [72]) one may write the Boltzmann equation for the electron distribution function $f_e(r, v, t)$ as

$$\frac{\partial f_e(r, v, t)}{\partial t} = \frac{e}{3mv^2} \frac{\partial}{\partial v} (v^2 \mathbf{E} \cdot \mathbf{f}_1) + \frac{1}{2v^2} \frac{\partial}{\partial v} (v^2 \delta v_{el}(v) [\frac{T}{m} \frac{\partial f_0}{\partial v} + v f_0]) + S_0, \quad (11a)$$

where

$$\frac{\partial f_1}{\partial t} = \frac{e \mathbf{E}}{m} \frac{\partial f_0}{\partial v} + \frac{e}{mc} [\mathbf{B}^0 \times \mathbf{f}_1] - \nu(v) f_1. \quad (11b)$$

Here $\nu(v)$ is the total electron-target collision frequency, δ is the fractional energy loss per collision, and $\nu_{el}(v)$ is the elastic collision frequency. The inelastic collision rates S_0 represent the details of the electron-target interaction, and include effects (where appropriate) of rotational (S_0^{rot}), vibrational (S_0^{vib}) and

electronic (S_0^{ele}) excitation; dissociation (S_0^{diss}), ionization (both direct and dissociative) (S_0^i), dissociative ionization (S_0^{di}), dissociative excitation (S_0^{de}); electron attachment (both direct and dissociative) (S_0^{at}) and electron-ion recombination (S_0^{rec}). Further details may be found in Refs. [74] and [76]. Results of the solutions to Eqs. (11a) and (11b) for $h = 90$ km are shown in Fig. 10 for the assumed electron and neutral densities. The initial condition was an electric field $E=10$ V/m applied for $20 \mu s$ starting at $t = 0$ sec.

As the electric field propagates upward from the cloud discharge it interacts with the ambient atmosphere to set up the electron densities and eedfs, such as shown in Fig. 10. The heated electrons interact with the ambient gas (mainly N_2 and O_2) to produce characteristic emission bands in elves, sprites, and blue jets. The principal bands are given in Table 1. A moderate-resolution spectrum of one red sprite is shown in Fig. 11. Prominent are bands in the $B \rightarrow A$ ($1P$) system. There may be traces of the $N_2^+ A \rightarrow X$ (Meinel) system, but the signal-to-background should be improved. The Meinel system is interesting in that its presence gives some indication of the highest electron energies present in the discharge. Thus, ionic features observed by Armstrong *et al.* [79], and not observed by Mende *et al.* [80] could be due to problems of resolution, aerosol scattering, and low signal-to-background; but also to eedfs in some more energetic sprites (larger E -field) having a higher-energy tail [81]. Future airborne campaigns should include a careful study of the Meinel system as a marker of electron energy.

A detailed study of the N_2 emission rates has been carried out by Morrill *et al.* [69] in which the QSE model [66] is used to calculate the electric fields, and solution to Boltzmann's equation to calculate the eedf as a function of altitude. Results for excitation of seven triplet state of N_2 are shown in Fig. 12 at $h = 65$ and 75 km. The temporal duration of the excitations may be understood in terms of the faster relaxation (higher conductivity,

see Fig. 9) of the E field at the higher altitude.

Less spectral information is available on elves. Shuttle observations were first made with broad-band cameras with a response peaking at 440 nm [82]. Broad-band filter/photometer measurements have been reported by Fukunishi et al. [83]. Taranenko et al. [81] calculated optical emission intensities from lines of N, N₂, N₂⁺, O, O₂ and O₂⁺. Estimate emission intensities were in the range 10⁰-10⁹ Rayleigh, with durations in the range 50 ns-350 ms after termination of the quasi-static electric field. Considering the relevant excitation and quenching rates, O₂ lines would be the most intense emitter as viewed from Shuttle or other spacecraft [81]. Moderate-to-high resolution optical spectra would be a needed component of any future elves campaign.

Given the interesting calculations of Milikh et al. [84] such a low-earth orbiting campaign should also include an infrared-measurement capability at 4.26 μm. Emission at 4.26 μm arises from the degenerate energy transfer between long-lived (optical emission is dipole-forbidden) vibrationally-excited N₂ (v") ("vibrons") and v"J" levels of CO₂ to give rise to the dipole-allowed emission CO₂ (001) → (000) at 4.26 μm (lifetime τ_{life} = 2.5 ms. A Fokker-Planck approximation to the Boltzmann equation is solved for the eedf. The eedf is then used to calculate excitation rates of N₂ (v"), the collisional transfer rates to CO₂, and the 4.26 μm photon escape rates from the optically thick atmosphere. An outline of the collision particles is given in Fig. 13. Relevant processes, starting with N₂^{*} are: N₂^{*} de-excitation by atomic O (k₂) and O₂ (k₃); vibron excitation by O₂^{*} (k₃'); vibron transfer to CO₂ (k₁) and back-transfer by CO₂^{*} to N₂ (k₁'); absorption by CO₂ of a previously-emitted 4.26 μm photon, and radiation of a 4.26 μm photon to the atmosphere with lifetime τ_{life} ; and O₂^{*} removal by quenching reactions with O (k₅) and H₂O (k₄). The excited H₂O can radiate its vibrational energy by dipole transition [85].

The excitation coefficients for the various N₂(v") levels and

for $\text{CO}_2(001)$ is shown in Fig. 14 as a function of the electron quiver energy (total electron energy, including linear translation as well as cyclotron energy). These rates are computed by averaging experimental electron-impact excitation cross sections for $\text{N}_2(v'')$ and $\text{CO}_2(001)$ over the calculated *eedf*. Interestingly, a millisecond-type EMP pulse will produce a delay in the IR emission for as long as 200 sec. Sources of the delay are the time for N_2 and CO_2 to find one another and transfer energy; and the time for the entrapped IR photons, starting at about 85 km, to diffuse upwards through the ionosphere.

Acknowledgments

This work was carried out at the Jet Propulsion Laboratory, California Institute of Technology, and was supported through the National Science Foundation under agreement with the National Aeronautics and Space Administration.

References

- [1] R. J. Strangeway, *Adv. Space Res.* 15, 89 (1995).
- [2] Y. Yair, Z. Levin and S. Tzivion, *J. Geophys. Res.* 103, 14157 (1998).
- [3] A. Chutjian, A. Garscadden and J. Wadehra, *Physics Reports* 264, 393 (1996).
- [4] A. Garscadden, *Pure and Appl. Chem.* 66, 1319 (1994).
- [5] O. Biham, I. Furman, N. Katz, V. Pirronello and G. Vidali, *Mon. Not. Royal Astron. Soc.* 296, 869 (1998).
- [6] A. A. Howling, J-L. Dorier and Ch. Hollenstein, *Appl. Phys. Lett.* 62, 1341 (1993).
- [7] A. A. Howling, L. Sansonnens, J-L. Dorier and Ch. Hollenstein, *J. Phys. D: Appl. Phys.* 26, 1003 (1993).
- [8] P. Kae-Nune, J. Perrin, J. Guillon and J. Jolly, *Jpn. J. Appl. Phys.* 33, 4303 (1994).
- [9] Y. Watanabe, M. Shiratani, T. Fukuzawa, H. Kawasaki, Y. Ueda, S. Singh and H. Ohkura, *J. Vac. Sci. Technol. A* 14, 995 (1996).
- [10] H. Kawasaki, H. Ohkura, T. Fukuzawa, M. Shiratani, Y. Watanabe, Y. Yamamoto, S. Suganuma, M. Hori and T. Goto, *Jpn. J. Appl. Phys.* 36, 4985 (1997).
- [11] H. Kawasaki, J. Kida, K. Sakamoto, T. Fukuzawa, M. Shiratani and Y. Watanabe, *Jpn. J. Appl. Phys.* 37, L475 (1998).
- [12] Y. Watanabe, M. Shiratani, H. Kawasaki, S. Singh, T. Fukuzawa, Y. Ueda and H. Ohkura, *J. Vac. Sci. Technol. A* 14, 540 (1996).
- [13] H. Kawasaki, K. Sakamoto, S. Maeda, T. Fukuzawa, M. Shiratani and Y. Watanabe, *Jpn. J. Appl. Phys.* 37, L1264 (1998).
- [14] H. Kawasaki, K. Sakamoto, S. Maeda, T. Fukuzawa, M. Shiratani and Y. Watanabe, *Jpn. J. Appl. Phys.* 37, 5757 (1998).
- [15] P. Kae-Nune, J. Perrin, J. Jolly and J. Guillon, *Surf. Sci.* 360, L495 (1996).
- [16] J. Perrin, M. Shiratani, P. Kae-Nune, H. Videlot, J. Jolly and J. Guillon, *J. Vac. Sci. Technol. A* 16, 278 (1998).
- [17] M. Shiratani, H. Kawasaki, T. Fukuzawa, Y. Watanabe, Y. Yamamoto, S. Suganuma, M. Hori and T. Goto, *J. Phys. D:*

- Appl. Phys.* 31, 776 (1998).
- [18] M. Shiratani, H. Kawasaki, T. Fukuzawa and Y. Watanabe, *Surf. Rev. and Letters* 3, 75 (1996).
 - [19] S. Gough, C. Schermann, F. Pichou, M. Landau, I. Čadež and R. I. Hall, *Astron. Astrophys.* 305, 687 (1996); C. Schermann, F. Pichou, M. Landau, I. Čadež and R. I. Hall, *J. Chem. Phys.* 101, 8152 (1994).
 - [20] J. R. Hiskes, *Appl. Phys. Letters* 57, 231 (1990).
 - [21] J. Perrin, O. Leroy and M. C. Bordage, *Contrib. Plasma Phys.* 36, 3 (1996).
 - [22] O. Leroy, G. Gousset, L. L. Alves, J. Perrin and J. Jolly, *Plasma Sources Sci. Technol.* 7, 348 (1998).
 - [23] M. Shiratani and Y. Watanabe, *Rev. Laser Engineering* 26, 449 (1998).
 - [24] H. Kawasaki, J. Kida, K. Sakamoto, T. Fukuzawa, M. Shiratani and Y. Watanabe, *J. Appl. Phys.* 83, 5665 (1998).
 - [25] M. Shiratani, H. Kawasaki, T. Fukuzawa and Y. Watanabe, *J. Vac. Sci. Technol. A* 14, 603 (1996).
 - [26] Y. Matsuoka, M. Shiratani, T. Fukuzawa, Y. Watanabe and K. Kim, *Bull. Am. Phys. Soc.* 43, 1423 (1998).
 - [27] D. M. Wood, *Phys. Rev. Lett.* 46, 749 (1981).
 - [28] Y. Liu, Q-L. Zhang, F. K. Tittel, R. F. Curl and R. E. Smalley, *J. Chem. Phys.* 85, 7434 (1986).
 - [29] T. Fukuzawa, K. Obata, H. Kawasaki, M. Shiratani and Y. Watanabe, *J. Appl. Phys.* 80, 3202 (1996).
 - [30] J. Perrin, P. Molinàs-Mata and P. Belenguer, *J. Phys. D: Appl. Phys.* 27, 2499 (1994).
 - [31] H. Ikezi, *Phys. Fluids* 29, 1764 (1986).
 - [32] H. Thomas, G. E. Morfill, V. Demmel, J. Goree, B. Feuerbacher and D. Möhlmann, *Phys. Rev. Letters* 73, 652 (1994).
 - [33] J. H. Chu and Lin I., *Phys. Rev. Letters* 72, 4009 (1994).
 - [34] D. H. E. Dubin, *Phys. Rev. A* 42, 4972 (1990).
 - [35] A. Melzer, T. Trottenberg and A. Piel, *Phys. Letters A* 191, 301 (1994).
 - [36] K. Takahashi, Y. Hayashi and K. Tachibana, *Bull. Am. Phys.*

- Soc. 43, 1482 (1998) (abstract NW3-3); Y. Hayashi and A. Sawai, *ibid.* (abstract NW3-4)
- [37] H. R. Snyder, M. S. Murillo, G. S. Selwyn and D. Winske, *Bull. Am. Phys. Soc.* 43, 1482 (1998) (abstract NW3-5).
- [38] H. C. Lee, D. Y. Chen and B. Rosenstein, *Phys. Rev. E* 56, 4596 (1997).
- [39] E. C. Whipple, T. G. Northrop and D. A. Mendis, *J. Geophys. Res.* 90, 7405 (1985); E. C. Whipple, *Rep. Prog. Phys.* 44, 1197 (1981).
- [40] C. K. Goertz, *Revs. Geophysics* 27, 271 (1989).
- [41] T. W. Hartquist, O. Havnes and G. E. Morfill, *Fund. Cosmic Physics* 15, 107 (1992).
- [42] M. Horanyi, *Adv. Space Res.* 13, 231 (1993).
- [43] T. W. Hartquist, W. Pillip and O. Havnes, *Astrophys. Space Sci.* 246, 243 (1997).
- [44] A. Owens, et al., *Astrophys. J.* 493, L47 (1998).
- [45] R. E. Johnson, *Space Science Revs.* 69, 215 (1994); ---, *Revs. Mod. Physics* 68, 305 (1996).
- [46] R. E. Johnson, R. M. Killen, J. H. Waite Jr. and W. S. Lewis, *Geophys. Res. Letters* 25, 3257 (1998).
- [47] G. Vidali, V. Pirronello, C. Liu and L. Shen, *Astro. Letters and Communications* 35, 423 (1998).
- [48] V. Pirronello, O. Biham, C. Liu, L. Shen and G. Vidali, *Ap. J.* 483, L131 (1997).
- [49] V. Pirronello, C. Liu, L. Shen and G. Vidali, *Ap. J.* 475, L69 (1997).
- [50] M. Horanyi and D. A. Mendis, *Earth, Moon, and Planets* 37, 71 (1987).
- [51] R. J. Gould and E. E. Salpeter, *Astrophys. J.* 138, 393 (1963).
- [52] D. Hollenbach and E. E. Salpeter, *Astrophys. J.* 163, 155 (1971); ----, *J. Chem. Phys.* 53, 79 (1970).
- [53] A. Zangwill, *Physics at Surfaces* (Cambridge, New York, 1988). See also L. W. Bruch, M. W. Cole and E. Zaremba, *Physical Adsorption: Forces and Phenomena* (Clarendon, Oxford, 1997).
- [54] A. Levinson, D. F. Chernoff and E. E. Salpeter, *Molecule Formation In and On Grains. I: Physical Regimes*, available

online at xxx.lanl.gov, manuscript astro-ph/9706251.

- [55] W. L. Boeck, O. H. Vaughan Jr., R. J. Blakeslee, B. Vonnegut and M. Brook, *J. Atm. Solar-Terrestrial Phys.* 60, 669 (1998).
- [56] D. D. Sentman, E. M. Wescott, D. L. Osborne, D. L. Hampton and M. J. Heavner, *Geophys. Res. Letters* 22, 1205 (1995).
- [57] D. D. Sentman and E. M. Wescott, *Phys. Plasma* 2, 2514 (1995).
- [58] C. T. R. Wilson, *Proc. Roy. Meteorol. Soc. London* 236, 297 (1956).
- [59] H. L. Rowland, R. F. Fernsler, J. D. Huba and P. A. Bernhardt, *Geophys. Res. Letters* 22, 361 (1995).
- [60] H. L. Rowland, R. F. Fernsler, and P. A. Bernhardt, *J. Geophys. Res.* 101, 7935 (1995).
- [61] R. F. Fernsler and H. L. Rowland, *J. Geophys. Res.* 101, 29653 (1996).
- [62] V. P. Pasko, U. S. Inan, Y. N. Taranenko and T. F. Bell, *Geophys. Res. Letters* 22, 365 (1995).
- [63] H. L. Rowland, *J. Atm. Solar-Terrestrial Phys.* 60, 831 (1998).
- [64] H. M. Wescott, D. D. Sentman, M. J. Heavner, D. L. Hampton and O. H. Vaughan Jr., *J. Atm. Solar-Terrestrial Phys.* 60, 713 (1998).
- [65] Z. Ma, C. L. Croskey and L. C. Hale, *J. Atm. Solar-Terrestrial Phys.* 60, 845 (1998).
- [66] V. P. Pasko, U. S. Inan, T. F. Bell and Y. N. Taranenko, *J. Geophys. Res.* 102, 4529 (1997).
- [67] E. M. Wescott, D. D. Sentman, M. J. Heavner, D. L. Hampton, D. L. Osborne and O. H. Vaughan Jr., *Geophys. Res. Letters* 23, 2153 (1996).
- [68] A. I. Sukhorukov and P. Stubbe, *J. Atm. Solar-Terrestrial Phys.* 60, 725 (1998).
- [69] J. S. Morrill, E. J. Bucsela, V. P. Pasko, S. L. Berg, M. J. Heavner, D. R. Moudry, W. M. Benesch, E. M. Wescott and D. D. Sentman, *J. Atm. Solar-Terrestrial Phys.* 60, 811 (1998).
- [70] G. J. Fishman, P. N. Bhat, R. Mallozzi, J. M. Horack, T. Koshut, C. Kouveliotou, G. N. Pendleton, C. A. Meegan, R. B. Wilson, W. S. Paciesas, S. J. Goodman and H. J. Christian, *Science* 264, 1313 (1994).

- [71] Y. Taranenko and R. Roussel-Dupré, *Geophys. Res. Letters* 23, 571 (1996).
- [72] A. V. Phelps and L. C. Pitchford, *Phys. Rev. A* 31, 2932 (1985); L. C. Pitchford, S. V. O'Neil and J. R. Rumble Jr., *Phys. Rev. A* 23, 294 (1981).
- [73] G. Milikh, J. A. Valdivia and K. Papadopoulos, *J. Atm. Solar-Terrestrial Phys.* 60, 907 (1998).
- [74] Y. N. Taranenko, U. S. Inan and T. F. Bell, *Geophys. Res. Letters* 20, 1539 (1993).
- [75] Y. N. Taranenko, U. S. Inan and T. F. Bell, *Geophys. Res. Letters* 20, 2675 (1993).
- [76] A. V. Gurevich, *Nonlinear Phenomena in the Ionosphere* (Springer-Verlag, New York, 1978).
- [77] D. L. Hampton, M. J. Heavner, E. M. Wescott and D. D. Sentman, *Geophys. Res. Letters* 23, 89 (1996).
- [78] B. D. Green, M. E. Fraser, W. T. Rawlins, L. Jeong, W. A. M. Blumberg, S. B. Mende, G. R. Swenson, D. L. Hampton, E. M. Wescott and D. D. Sentman, *Geophys. Res. Letters* 23, 2161 (1996).
- [79] R. A. Armstrong, J. Shorter, W. A. Lyons, L. Jeong and W. A. M. Blumberg, *Eos Trans. AGU Fall Meeting*, Abstract A41D-5 (1995).
- [80] S. B. Mende, R. L. Rairden, G. R. Swenson and W. A. Lyons, *Geophys. Res. Letters* 22, 2635 (1995).
- [81] Y. N. Taranenko, U. S. Inan and T. F. Bell, *Geophys. Res. Letters* 19, 1815 (1992).
- [82] W. L. Boeck, O. H. Vaughan Jr., R. Blakeslee, B. Vonnegut and M. Brook, *Geophys. Res. Letters* 19, 99 (1992).
- [83] H. Fukunishi, Y. Takahashi, M. Kubota, K. Sakanoi, U. S. Inan and W. A. Lyons, *Geophys. Res. Letters* 23, 2157 (1996).
- [84] G. M. Milikh, D. A. Usikov and J. A. Valdivia, *J. Atm. Solar-Terrestrial Phys.* 60, 895 (1998).
- [85] J. K. Kumer and T. C. James, *J. Geophys. Res.* 79, 638 (1974).

Table 1. Frequently-Observed Molecular Transitions and Processes Relevant to Upward-Directed Discharges

Species	Transition	System/Process Description
N ₂	B ³ Π _g → A ³ Σ _u ⁺	first positive (1P) (red)
N ₂	C ³ Π _u → B ³ Π _g	second positive (2P) (blue)
N ₂	v" = 1 → v" = 0	vibrational-energy transfer to pump 4.26 μm radiation in CO ₂
N ₂ ⁺	B ² Σ _u → X ² Σ _g ⁺	first negative (1N) (blue)
N ₂ ⁺	A ² Π _u → X ² Σ _g ⁺	Meinel (red)
O ₂	e + O ₂ → O + O ⁻	dissociative attachment
O ₂	b ⁴ Σ _g ⁻ → a ⁴ Π _u	first negative (1N) (red)
O	O(¹ D) → O(³ P)	630.205 nm emission (red)
O	O(¹ S) → O(¹ D)	557.889 nm emission (green)
CO ₂	(001) → (000)	vibrational emission of 4.26 μm radiation

Figure Captions

Figure 1.

Experimental arrangement of the radiofrequency reactor (R) and Ar-ion laser to measure laser light-scattering from suspended dust particles in various reactant mixtures [23].

Figure 2.

Spatial distributions of intensities of Ar, Ge, and GeH_2 emissions, along with total particle amount, in a GeH_4 (10%O)-Ar RF discharge (6.5 MHz, 80W, 13 Pa) [11].

Figure 3.

Micrographs and representations of (a) hexagonal, (b) bcc, and (c) fcc crystal lattices in an O_2 - SiH_4 RF reactor [33]. Shaded areas in the sketch are planes normal to the optical viewing axis of the system. Blurred images are from particles in the slightly out-of-focus third plane.

Figure 4.

Measured charge on suspended TiO_2 particles of 18 μm diameter, as a function of peak-to-peak RF voltage. Analysis follows from Eq. (5) where measurements are made from the oscillation amplitude factor (Δ) or from the resonance frequency (O) [35].

Figure 5.

Hubble Space Telescope photograph of a star nursery in the Eagle Nebula. The pillar-like structures are columns of gas and dust, within which new stars have recently been formed. The column at the left is one light year in length. Small globules of denser gas and dust (EGGS, or evaporating gaseous globules) are buried within the lower-density pillars. Photo credit: J. Hester and P. Scowen (Arizona State Univ.) and NASA.

Figure 6.

Schematic diagram of a two-beam apparatus to study H_2 formation on grains. Separate beams of H and D atoms are produced in an RF

source, with about 70-85% dissociation of the feed H_2 and D_2 gases. The collimated, differentially-pumped thermal-energy beams of H and D atoms are brought to the UHV scattering chamber where they are adsorbed onto a grain sample (olivine, pyrolytic graphite, etc.). The HD and D_2 produced on the surface are desorbed using temperature-programmed desorption (TPD), and detected by the quadrupole mass selector (QMS) [5].

Figure 7.

Typical temperature-programmed desorption curve for HD from an olivine surface as a function of surface temperature. Curves are for exposure times to the H and D beams of (bottom to top) 0.07, 0.1, 0.25 and 0.55 minute [48].

Figure 8.

Schematic of various phenomena (top) and mechanisms (bottom) of lightning-ionospheric interactions, as a function of altitude. Phenomena can give rise to alterations (Δ) in optical emissions ($\Delta h\nu$), atmospheric temperature (ΔT), and electron density (ΔN_e) detected as scattering of VLF signals. Other abbreviations are cloud-to-ground discharges (CG), quasistatic electric (QSE) fields and heating, electromagnetic pulse (EMP), and spacecraft (S/C) [66].

Figure 9.

Atmospheric electrical conductivity profiles σ for three latitudes and times. The relaxation time τ_r is given by ϵ_0/σ , and $\omega = 1/\tau_r$ [65].

Figure 10.

Ionospheric characteristics and results from Boltzmann-equation calculations in Eqs.(11a) and (11b) [74]. Upper left: profiles of ambient electron and neutral densities. Electron densities are shown for (a) nighttime, (b) intermediate, and (c) daytime. At an altitude of 90 km, shown are upper right: eedfs at the indicated times after start of the E field. lower left:

normalized electron current density and average electron energy; *lower right*: total gaseous attachment and ionization rates as a function of time after discharge.

Figure 11.

Synthetic sprite spectrum [77] with a computed fit (heavier line) using the emission systems indicated. Response-corrected sprite spectrum recorded at the Mt. Evans Observatory in Colorado is shown with lighter/broken lines [78].

Figure 12.

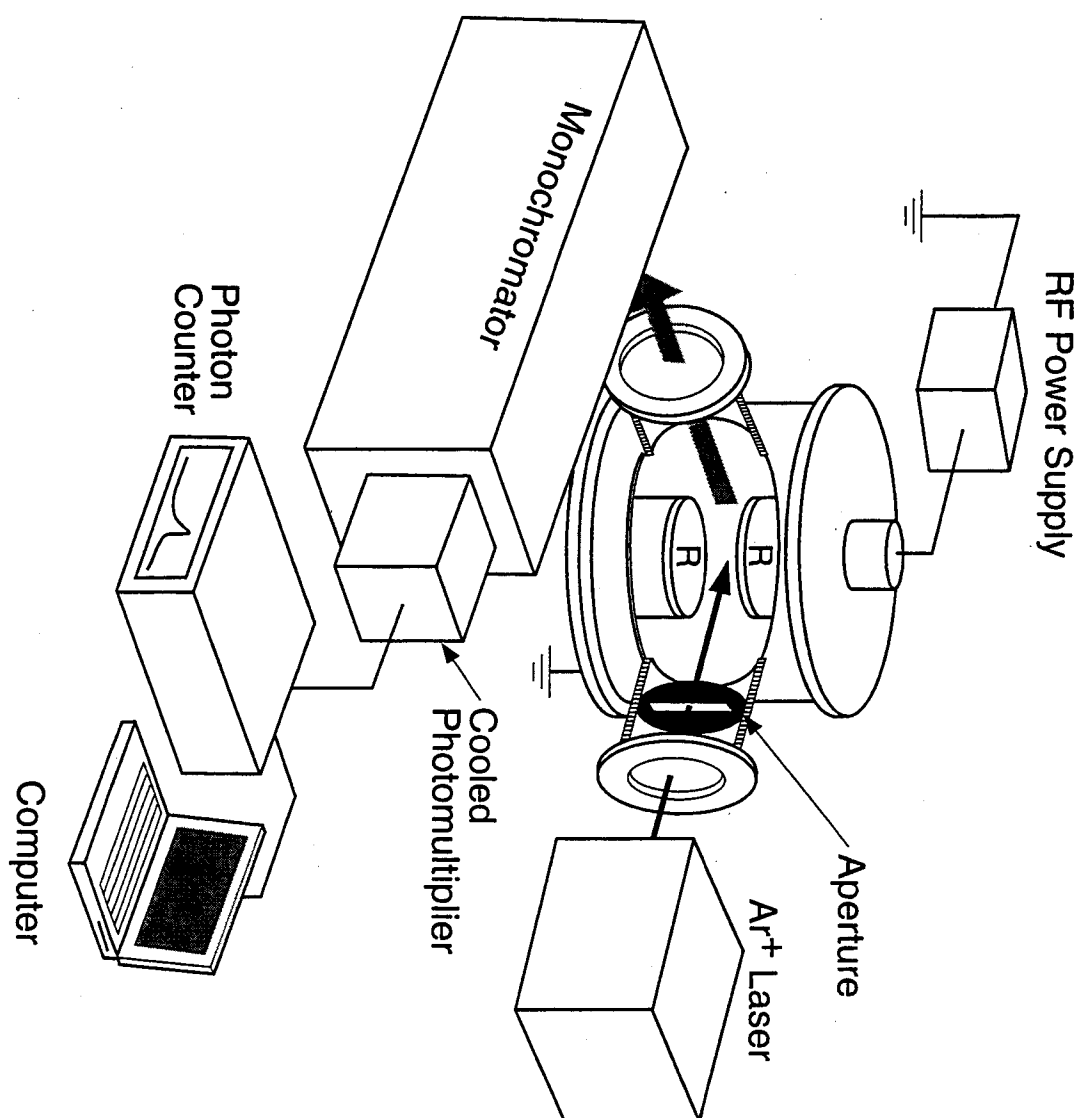
Production rate of seven triplet states of N_2 as a function of time after initiation of the quasi-static field. Results are shown at altitudes of 65 km and 75 km [69]. The notation refers to the states A $^3\Sigma_u^+$, B $^3\Pi_g$, W $^3\Delta_u$, B' $^3\Sigma_u^-$, C $^3\Pi_u$, D $^3\Sigma_u^+$ and E $^3\Sigma_g^+$.

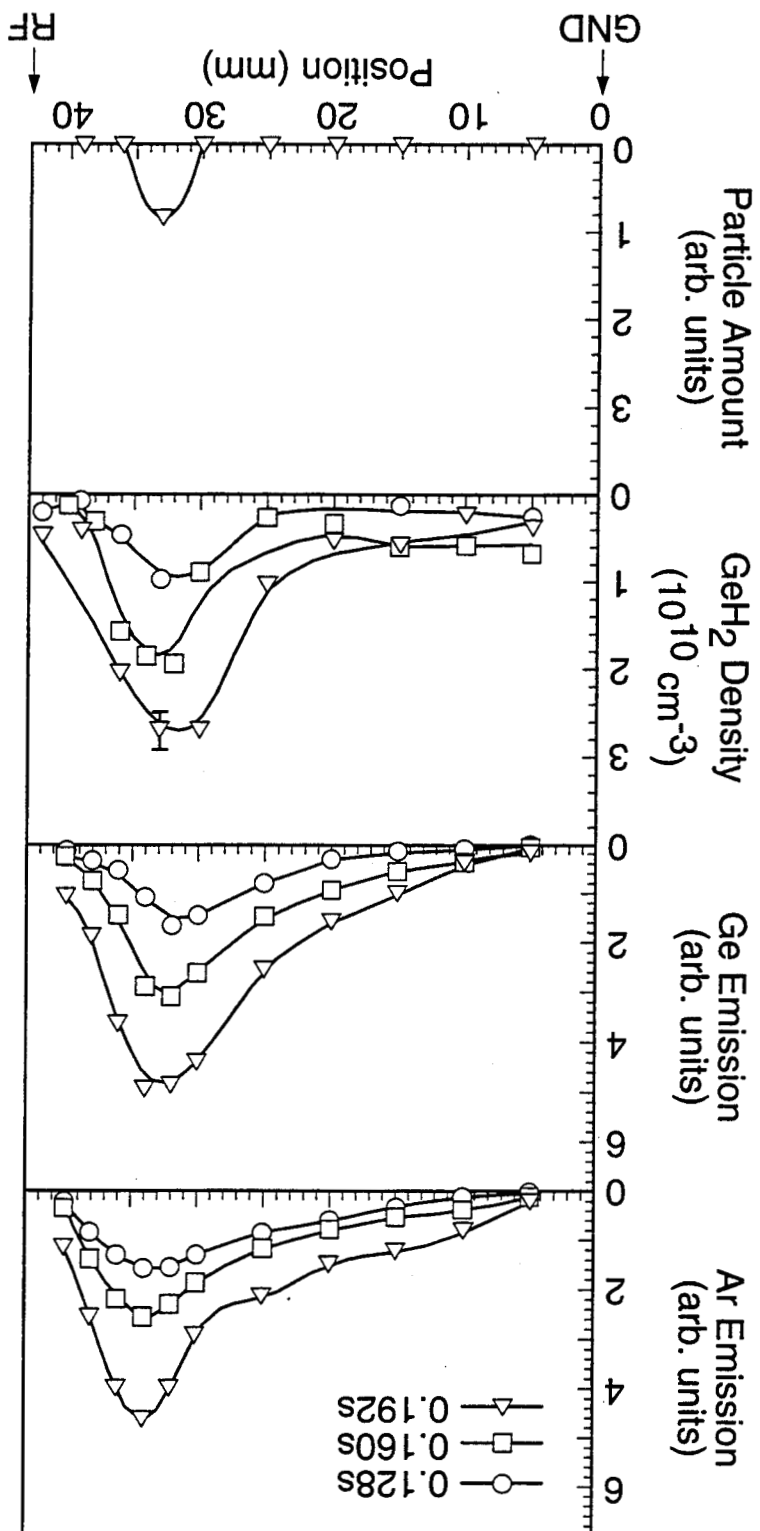
Figure 13.

Schematic representation of the reaction pathways for vibrons, $N_2(v''=1)$, produced by lightning discharges in the upper atmosphere [84].

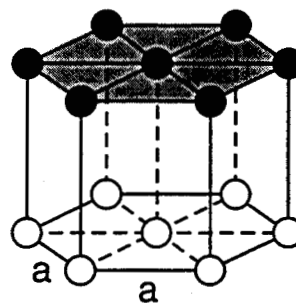
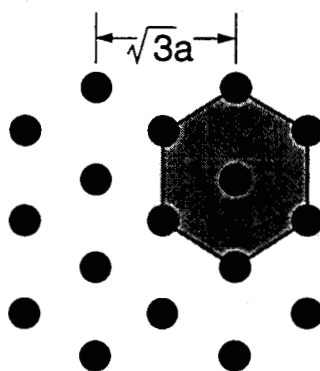
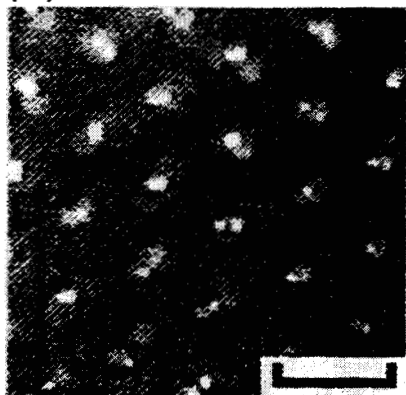
Figure 14.

Excitation rate coefficient of vibrational levels v'' in N_2 (solid lines), the effective rate for all levels (dotted line), and the excitation rate coefficient for $CO_2(001)$ (broken line) [84].

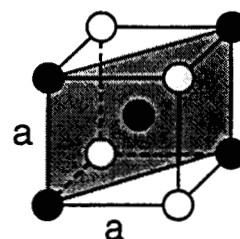
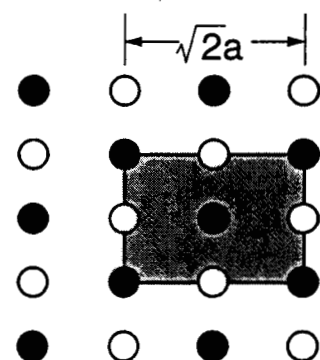
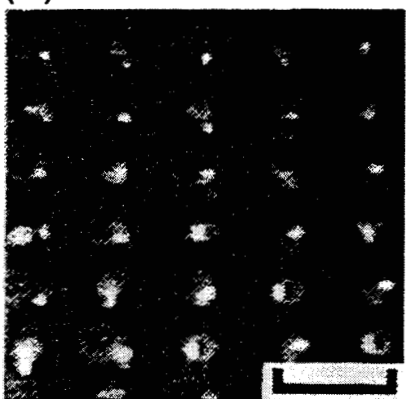




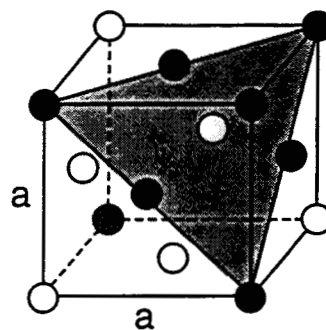
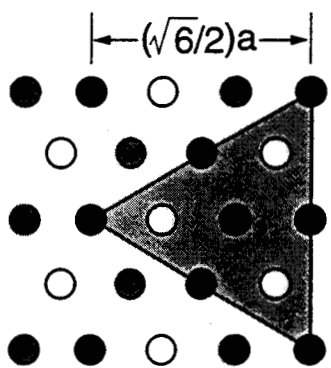
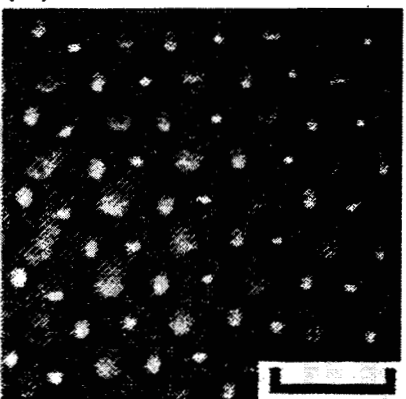
(a)



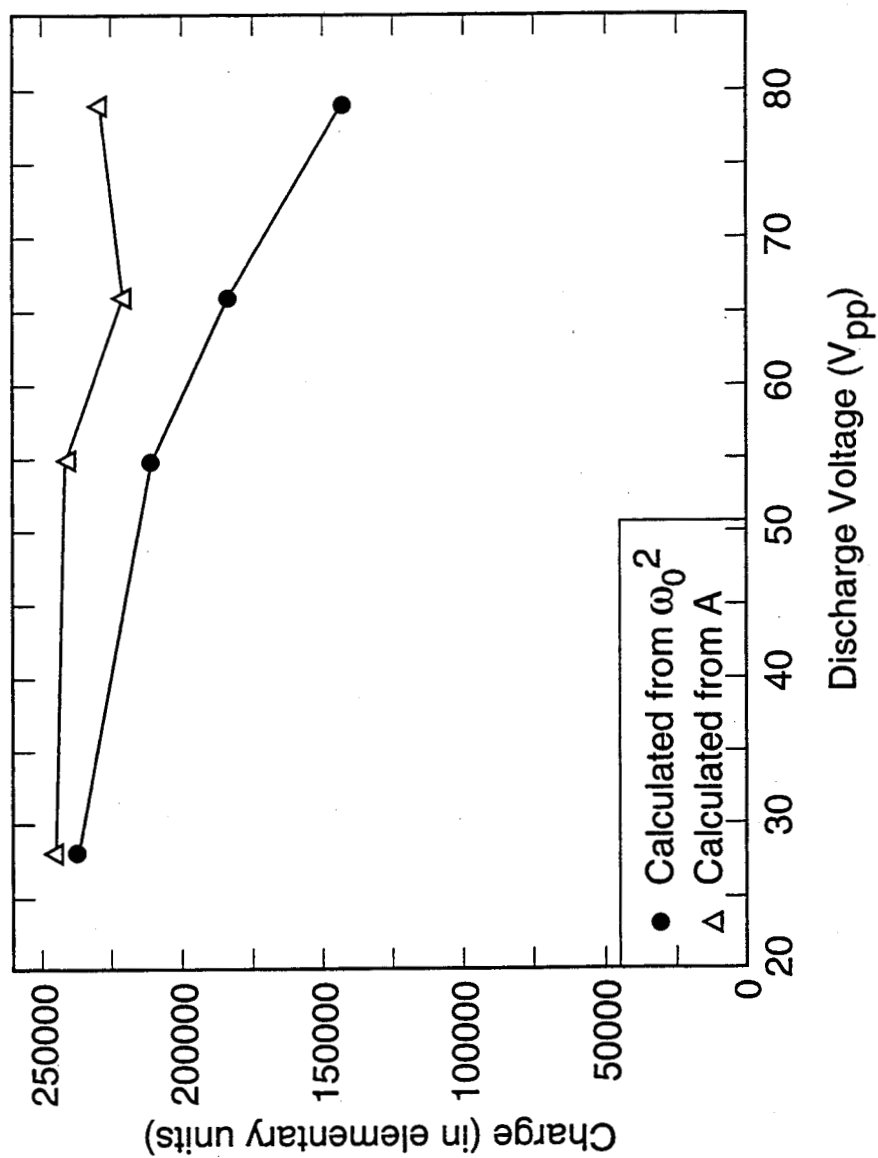
(b)



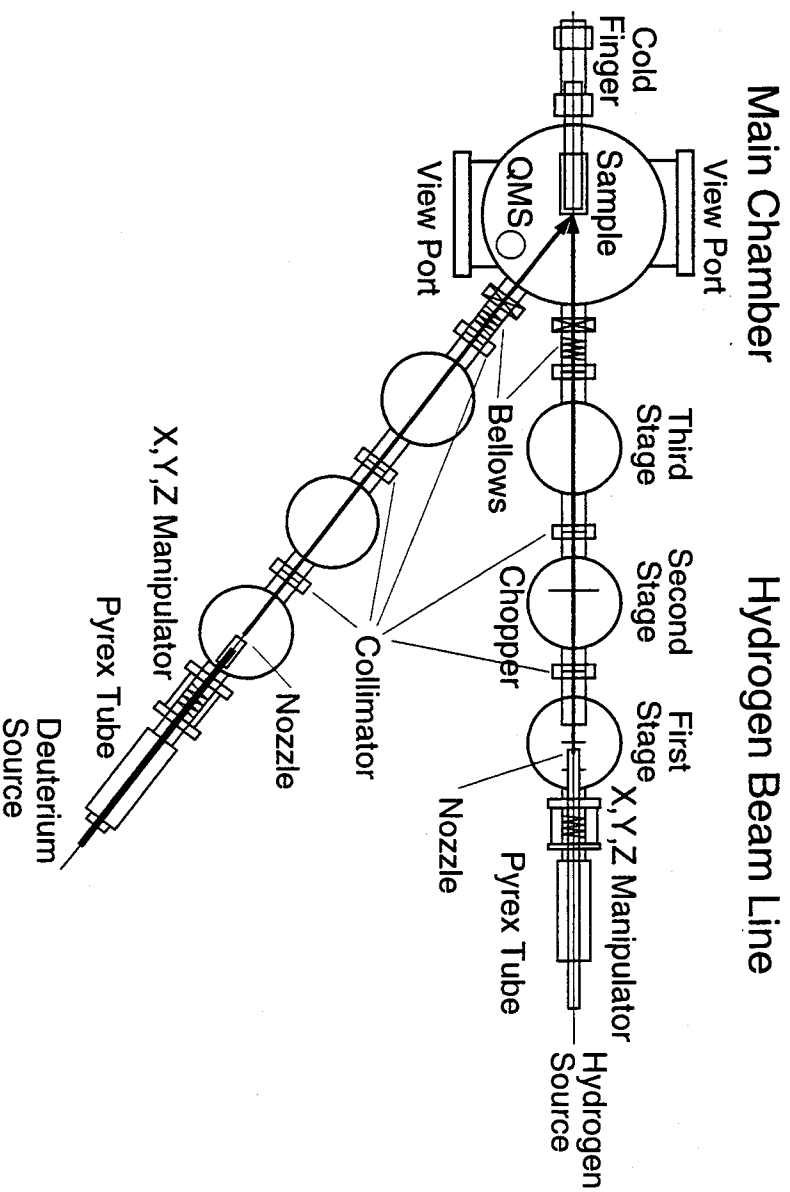
(c)



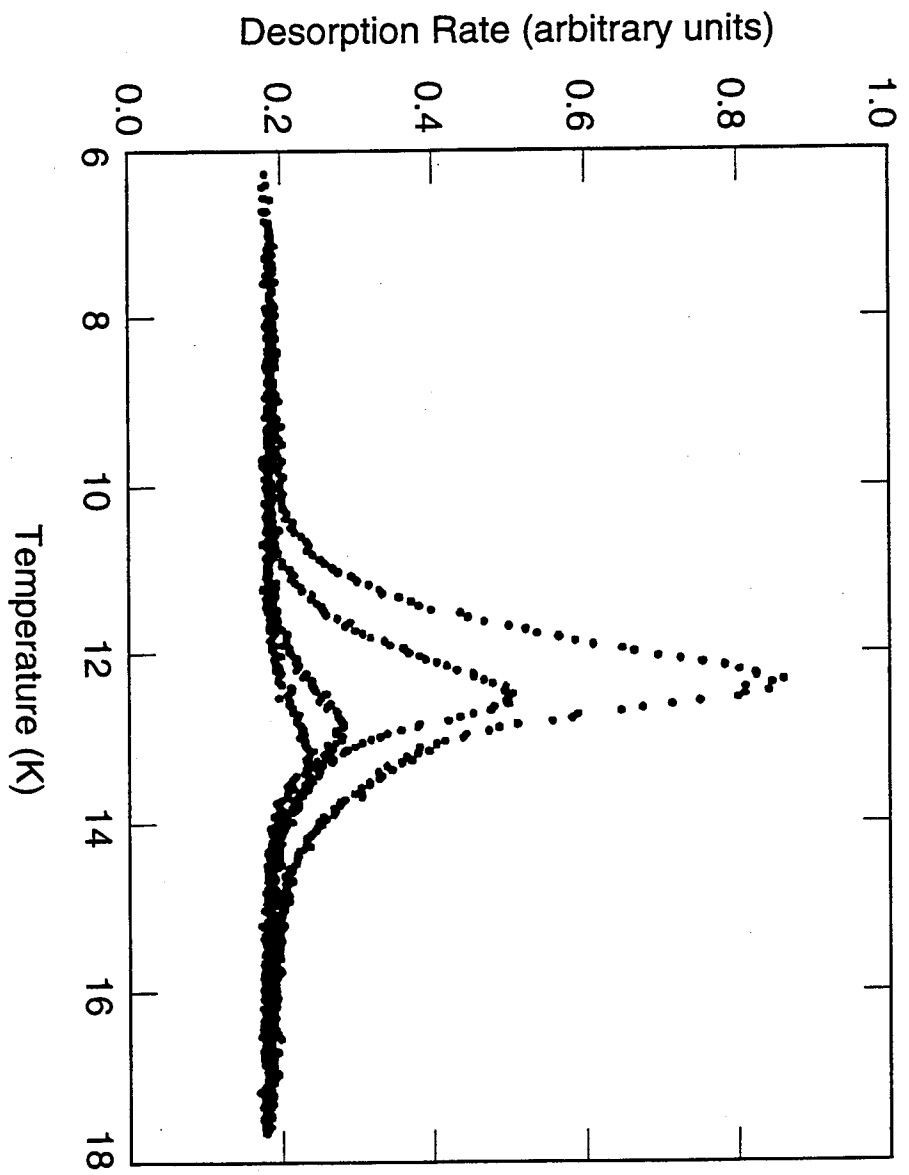
●: 1st layer ○: 2nd layer ●: 3rd layer



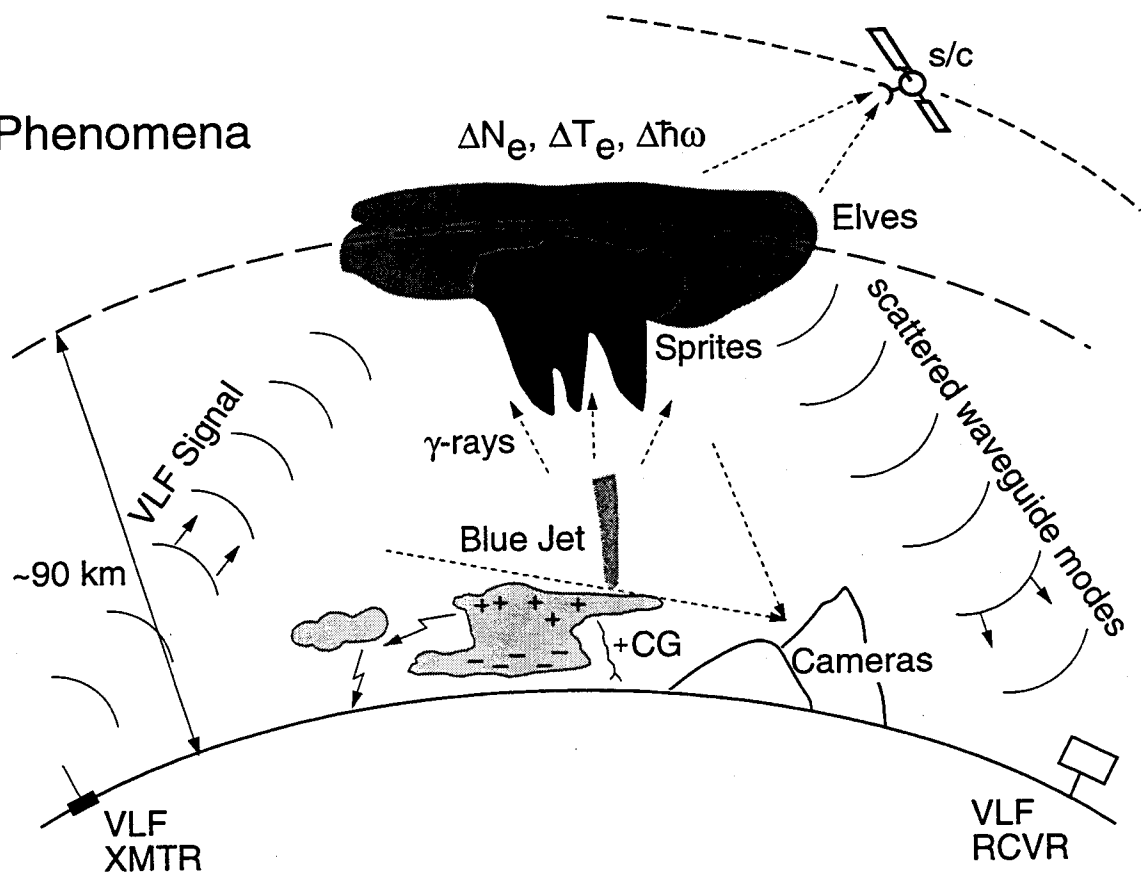




Deuterium Beam Line



Phenomena



Mechanisms

